ADVANCED MATERIALS
www.advmat.de

A Morphologically Stable Li/Electrolyte Interface for All-Solid-State Batteries Enabled by 3D-Micropatterned Garnet

*Rong Xu, Fang Liu, Yusheng Ye, Hao Chen, Rachel Rae Yang, Yinxing Ma, Wenxiao Huang, Jiayu Wan, and Yi Cui**

Morphological degradation at the Li/solid-state electrolyte (SSE) interface is a prevalent issue causing performance fading of all-solid-state batteries (ASSBs). To maintain the interfacial integrity, most ASSBs are operated under low current density with considerable stack pressure, which significantly limits their widespread usage. Herein, a novel 3D-micropatterned SSE (3D-SSE) that can stabilize the morphology of the Li/SSE interface even under relatively high current density and limited stack pressure is reported. Under the pressure of 1.0 MPa, the Li symmetric cell using a garnet-type 3D-SSE fabricated by laser machining shows a high critical current density of 0.7 mA cm^{-2} and stable cycling over 500 h under 0.5 mA cm^{-2}. This excellent performance is attributed to the reduced local current density and amplified mechanical stress at the Li/3D-SSE interface. These two effects can benefit the flux balance between Li stripping and creep at the interface, thereby preventing interfacial degradation such as void formation and dendrite growth.

1. Introduction

Rechargeable Li-ion batteries (LIBs) have enabled the widespread use of portable electronic devices and electric vehicles (EVs).[1–3] However, satisfying the rapidly growing demand from the EV industry on energy density is challenging for current LIB technology.[4,5] With the highest specific energy density (3860 mAh g^{-1}) and the lowest electrochemical potential (−3.04 V), Li-metal anode offers a potential solution to overcome this challenge.[6,7] Neverthless, the Li-metal anode has yet to be adopted in practical batteries because of its high reactivity against the conventional liquid electrolytes.[8] The use of inorganic solid-state electrolyte (SSE) is predicted as an effective approach to enable the stable service of Li-metal anode by inhibiting the consumptive side reactions at the Li/electrolyte interface and suppressing the growth of Li dendrites.[9,10] However, all-solid-state batteries (ASSBs) using the inorganic SSE and Li-metal anode still experience issues with dendrite penetration and associated early short-circuit during battery operation.[11–14] So far, considerable efforts have been devoted to elucidating the underlying mechanisms of this early failure of ASSBs.[15–18] It is generally acknowledged that the dynamic morphological evolution at the Li/SSE interface can remarkably influence the electrochemical performance of ASSBs.[17,19–23] In specific, during striping, Li atoms at the Li/SSE interface dissolve into SSE, and meanwhile, the diffusion of Li atoms in Li metal replenishes the Li loss from the interface. Since the rate of Li striping usually exceeds the diffusion limit of Li atoms, the Kirkendall voids will initiate and grow at the interface, leading to the loss of interfacial contact and increased cell impedance.[20,24,25] The morphological degradation becomes even worse during the subsequent plating. Li prefers to deposit at the regions still contacted with SSE instead of the detached areas, which develops a nonuniform deposition at the interface that further promotes the nucleation and growth of Li dendrites as well as the short-circuit of ASSBs.[22,26]

An effective strategy to inhibit morphological degradation at the Li/SSE interface is applying an external stack pressure on ASSBs.[20–22] With the pressure, Li metal near the interface can mechanically deform through creep, offering another route to replenish the Li loss and thus prevent the void formation.[21,27] Nevertheless, the practical adoption of this strategy is limited by a strict constraint from the "critical stack pressure."[20] In specific, the applied pressure has to be higher than the "critical stack pressure" to effectively suppress the morphological degradation at the interface. Otherwise, the mechanical deformation will be slower than the electrochemical deformation caused by Li stripping, leading to an insufficient Li replenishment to the interface. In this case, the voids will still form at the interface, followed by the nucleation and growth of Li dendrites (**Figure 1**a). It should be noticed that the "critical stack pressure" can reach several MPa for the ASSBs cycled under relatively low current density (e.g., 7.5 MPa for the Li/garnet/Li cell cycled under 0.2 mA cm^{-2}).[20,21,28] This high stack pressure is out of range of the current LIB operation platform (0.1–1.0 MPa) [29] and also sets constraints on the robustness of SSE and thus the broad adoption of viable SSE.[29] Moreover, it is possible that the pressure of this magnitude acts as one

R. Xu, F. Liu, Y. Ye, H. Chen, R. R. Yang, Y. Ma, W. Huang, J. Wan, Y. Cui
Department of Materials Science and Engineering
Stanford University
Stanford, CA 94305, USA
E-mail: yicui@stanford.edu
R. R. Yang
The College Preparatory School
Oakland, CA 94618, USA
Y. Cui
Stanford Institute for Materials and Energy Sciences
SLAC National Accelerator Laboratory
Menlo Park, CA 94025, USA

DOI: 10.1002/adma.202104009

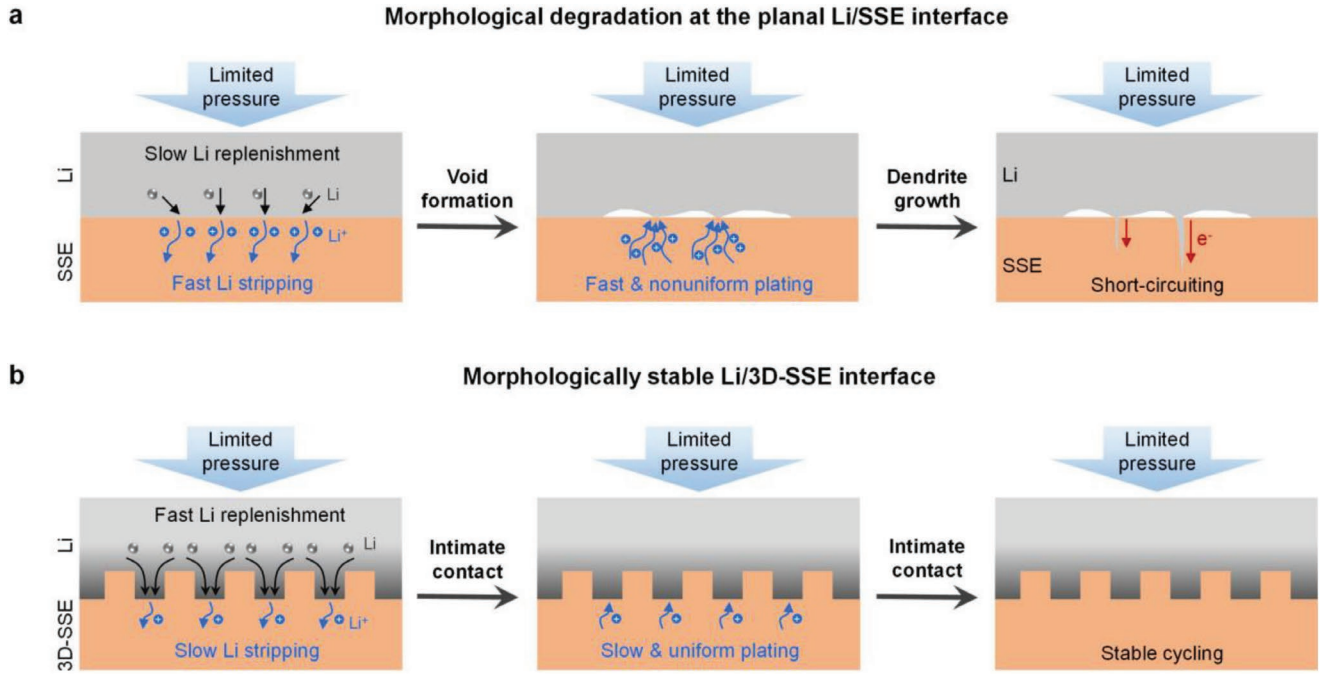

Figure 1. Schematic of the morphological evolution at the interface. a) When the cell is cycled under high current density and limited pressure, voids will form at the planar Li/SSE interface, followed by the nucleation and growth of Li dendrites. b) The Li/3D-SSE interface experiences a lower local current density and amplified mechanical stress, both of which prevent the morphological degradation at the interface.

of the driving forces for the dendrite propagation in SSE and promotes the short-circuit of ASSBs.[30,31] Considering all these limitations, we believe that a new strategy that can stabilize the morphology of the Li/SSE interface without using high stack pressure is urgently demanded.

Herein, we report a novel 3D-micropatterned SSE (3D-SSE) that can form a morphologically stable interface with Li metal even under relatively high current density and limited stack pressure. This 3D-SSE affords two critical effects compared to the conventional planar SSE. From an electrochemical perspective, the 3D-SSE with increased effective contact area with Li can lower the local current density to retard the Li stripping at the interface. From a mechanics perspective, it introduces a stress amplifying effect to facilitate the Li creep near the interface. Attributing to these two effects, the Li flux toward the interface driven by fast creep can become sufficient to replenish the Li loss by slow stripping, which prevents interfacial degradation during cell cycling (Figure 1b). We demonstrate that under limited pressure of 1.0 MPa, the Li symmetric cell using a garnet-type 3D-SSE exhibits a high critical current density (CCD) of 0.7 mA cm^{-2} and can stably operate over 500 h under 0.5 mA cm^{-2} without presenting significant interfacial degradation and early short circuit. In addition, we perform finite element analysis to elucidate the competition between electrochemistry and mechanics at the Li/SSE interface, which provides guidelines toward the future design of dendrite-free ASSBs.

2. Material Fabrication and Characterization

A garnet-type SSE (Ta-doped $Li_7La_3Zr_2O_{12}$, LLZO) is used as a model system in this work because of its high ionic conductivity, high elastic modulus, and more importantly, excellent stability against Li metal.[32,33] **Figure 2**a describes the fabrication process of the Li/3D-SSE/Li cells. First, a dense LLZO pellet is prepared by hot-press sintering. The fracture surface (Figure 2b) of the sintered pellet indicates its very low porosity, consistent with its high relative density of 98.0 ± 1.0% measured by the Archimedes method. X-ray diffraction (XRD) pattern shows that only cubic phase LLZO (c-LLZO) is present in the pellet (Figure 2c). Since the *c*-LLZO has favorable Li-ion transport pathways, the LLZO pellet presents a high ionic conductivity of 0.79 mS cm^{-1} at room temperature and low activation energy of 0.24 eV (Figure 2d and Figure S1, Supporting Information), both of which agree with previously reported values.[34]

The LLZO pellet is further micropatterned using a high-precision laser cutter to form the 3D-SSE (Figure 2e). The resolution of the laser cutter (20 µm) is one order of magnitude smaller than the characteristic dimensions of the 3D micropatterns (200–400 µm, Figure S2a, Supporting Information), which ensures a precise control on the shape of patterns. Technical parameters for the patterning, including output energy, translational speed, and cycle number, have been optimized to balance the processing time and quality. For instance, using a high-energy laser beam (400 ns pulse duration) can shorten the processing time but incur mechanical damage and undesirable chemical composition changes in the 3D-SSE (Figure S3, Supporting Information). After patterning, the 3D-SSE is examined again by XRD to verify the phase purity (Figure 2c). X-ray photoelectron spectroscopy (XPS) analysis further confirms the same chemical composition on the surfaces of 3D-SSE before and after patterning (Figure S4, Supporting Information). Note that a thin layer of contaminations (Li_2CO_3 and LiOH) might form on the surfaces of 3D-SSE during patterning, but most

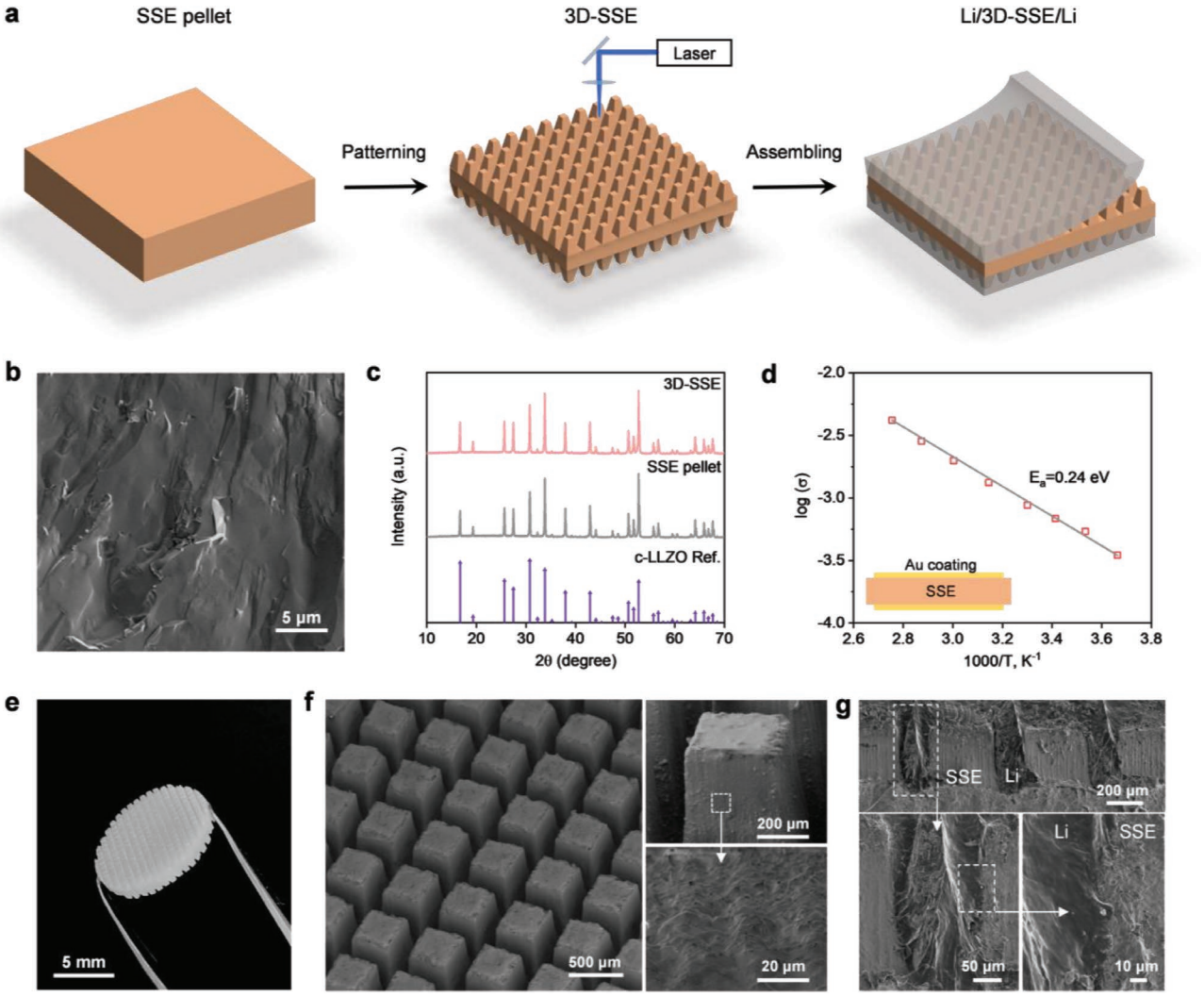

Figure 2. Fabrication and characterization of Li/3D-SSE/Li cell. a) Schematic of the fabrication process of Li/3D-SSE/Li cell. b) SEM images of the fracture surface of SSE pellet. c) XRD patterns of the SSE pellet and 3D-SSE. d) Ionic conductivity of the SSE pellet at different temperatures. e) A digital photo of the 3D-SSE. f) SEM images of the 3D-SSE. Enlarged images confirm that no significant mechanical damage is generated by laser cutting. g) Cross-sectional SEM images of the Li/3D-SSE/Li cell. Li metal forms an intimate contact with the 3D-SSE.

contaminations can be removed by the thermal treatment in the glovebox before assembling the cells (Figure S4, Supporting Information).[35] Scanning electron microscopy (SEM) and optical microscopy images show that no considerable material damage, such as cracks, has been generated in the 3D-SSE (Figure 2f and Figure S2b, Supporting Information). The uniaxial compression test also demonstrates that the 3D-SSE has excellent mechanical strength and can sustain a stack pressure (>12 MPa) far higher than the required stack pressure for cell operation (Figure S5, Supporting Information).

Li/3D-SSE/Li symmetric cells are assembled by sandwiching the 3D-SSE between two Li-metal chips. As the garnet SSE usually shows a lithiophobic nature to Li metal, simply sandwiching the Li metal with our 3D-SSE might leave some initial gaps at their interface.[36] Therefore, we utilize the low-temperature hot pressing at 160 °C to improve the initial contact between Li metal and 3D-SSE. Another strategy to overcome the poor wettability between Li metal and 3D-SSE is to construct a lithiophilic coating on the 3D-SSE surface such as ZnO, Au, or carbon composites, as demonstrated by many prior works.[37,38] The cross-sectional SEM images show that the Li metal forms an intimate contact with the 3D-SSE (Figure 2g). Based on the surface area of 3D SSE, the effective contact area between Li and 3D-SSE in the Li/3D-SSE/Li cells is around 2.5 times that in control Li/SSE/Li cells. It should be noted that the effective contact area in our design is not comparable with that in the recently proposed designs of 3D porous SSE.[39–41] The latter is to construct a 3D solid host with a high internal surface area for Li striping/plating, and thus the local current density can be significantly reduced. Differently, our design focuses more on constructing a 3D interface between Li metal and garnet SSE. Therefore, many issues associated with the 3D host designs can be avoided, such as the residual dead Li caused by the discontinuity or high tortuosity of 3D channels and the complexity for Li infiltration into the host (usually require ALD coating). The impedance of pristine Li/3D-SSE/Li and Li/SSE/Li cells

are measured by electrochemical impedance spectroscopy (EIS). The EIS spectra are fitted by two RC circuits in series representing the bulk and interfacial impedances, respectively (Figure S6, Supporting Information). The fitted bulk resistances for Li/3D-SSE/Li (129.1 Ω cm^2) and Li/SSE/Li cells (132.6 Ω cm^2) are close due to their similar thicknesses, while their interfacial resistances (16.9 and 50.4 Ω cm^2) are different because of the different effective contact areas. The Li/3D-SSE/Li cell with a higher effective contact area exhibits a lower interfacial resistance.

3. Electrochemical Performance

We first carry out the CCD testing with Li/3D-SSE/Li and Li/SSE/Li cells. During the testing, constant pressure of 1.0 MPa is applied on the cells, and the current density increases stepwise from 0.05 to 0.7 mA cm^{-2} (**Figure 3**a,b). Under low current densities, cell voltage in each galvanostatic cycle remains almost constant and follows Ohm's law. When the current density reaches the CCD, the voltage suddenly drops to around 0 V, indicating a short circuit between two Li electrodes. The CCD for Li/SSE/Li cell is 0.3 mA cm^{-2}, close to the values reported in the literature.[20,42] It reveals that the Li creep driven by the pressure of 1.0 MPa can merely replenish the Li stripped from the planar Li/SSE interface at a rate of 0.3 mA cm^{-2}, while further increasing the stripping rate can damage the interfacial morphology and cause the short circuit. In contrast, the Li/3D-SSE/Li cell can sustain a higher current density of 0.7 mA cm^{-2}. This is because the 3D-SSE can lower the local current density and amplify the local mechanical stress at the Li/3D-SSE interface, both of which are beneficial for the flux balance between Li stripping and creep, and thus prevent the void formation and subsequent dendrite nucleation at the interface. During the

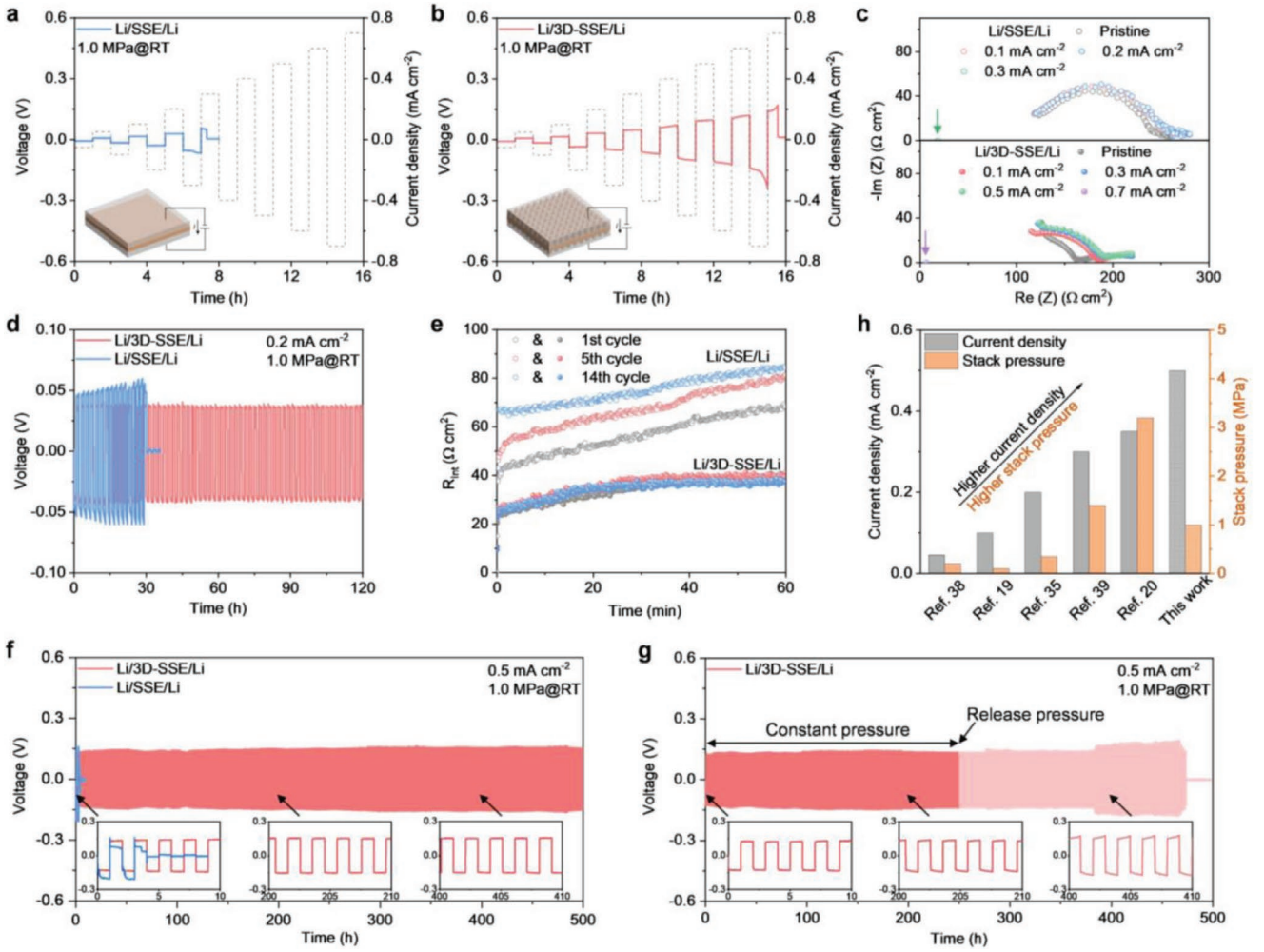

Figure 3. Electrochemical performance of Li/SSE/Li and Li/3D-SSE/Li cells. a,b) CCD testing on the Li/SSE/Li (a) and Li/3D-SSE/Li (b) cells with current steps from 0.05 to 0.7 mA cm^{-2}. c) EIS spectra of the Li/SSE/Li and Li/3D-SSE/Li cells cycled after different current steps in the CCD testing. d) Galvanostatic cycling of the Li/SSE/Li and Li/3D-SSE/Li cells under 0.2 mA cm^{-2} and 1.0 MPa. e) Evolution of the interfacial resistance in the Li/SSE/Li and Li/3D-SSE/Li cells. f) Long-term cycling of the Li/SSE/Li and Li/3D-SSE/Li cells under 0.5 mA cm^{-2} and 1.0 MPa. g) Long-term cycling of the Li/3D-SSE/Li cell under a releasing pressure. Insets in (f) and (g) show an enlarged view of the voltage profiles in 0–10, 200–210, and 400–410 h. h) Comparison of the cycling current density and required stack pressure of Li symmetric cells with conventional planar SSEs[19,20,35,38,39] and with a 3D-SSE in this work.

CCD testing, we obtain the EIS spectra for the cells cycled after each current step, as shown in Figure 3c. When the 3D-SSE replaces the planar SSE, the CCD at which the short circuit occurs increases from 0.3 to 0.7 mA cm^{-2}, which again confirms the improved dendrite resistance of the Li/3D-SSE interface.

The cyclability of Li/SSE/Li and Li/3D-SSE/Li cells is evaluated by the galvanostatic cycling under a current density of 0.2 mA cm^{-2} (0.2 mAh cm^{-2}) and limited stack pressure of 1.0 MPa. We observe two distinct features in the voltage profile of the Li/SSE/Li cell (Figure 3d and Figure S7, Supporting Information). First, within each cycle, the voltage gradually increases during charge and discharge (from 45 mV at the beginning of first discharge to 55 mV at the end of first discharge); Second, the voltage polarization accumulates as cycling proceeds (from ≈50 mV in the first cycle to ≈60 mV in the 14th cycle). When the voltage polarization reaches a certain level, an early short-circuit occurs in the Li/SSE/Li cell at the 30th hour of cycling. In contrast, the Li/3D-SSE/Li cell can continuously operate over 120 h with a constant voltage plateau of ≈45 mV. It is generally accepted that voltage polarization is correlated with increased cell resistance.[19,43] Before the short-circuit occurs, bulk resistances of the SSE and 3D-SSE should remain the same during cycling. Therefore, the voltage polarization is mainly attributed to the increase of interfacial resistance R_{int} caused by interfacial degradation. To track the evolution of R_{int} during cell cycling, we calculate the values of R_{int} from the voltage profiles in Figure 3d by extracting the contribution of bulk resistances. As shown in Figure 3e, R_{int} is only 39.5 Ω cm^2 for the pristine Li/SSE/Li cell yet increases to 69.1 Ω cm^2 after the first discharge. Moreover, the R_{int} keeps growing in the following cycles until the short-circuit occurs, indicating the continuous degradation of the Li/SSE interface. For the Li/3D-SSE/Li cell, R_{int} remains almost constant during the entire cycling, which highly emphasizes the capability of the Li/3D-SSE interface to suppress the interfacial degradation.

We also examine the long-term electrochemical performance of Li/SSE/Li and Li/3D-SSE/Li cells under a more practical current density of 0.5 mA cm^{-2} (0.5 mAh cm^{-2}) and the same constant pressure of 1.0 MPa. The Li/SSE/Li cell can hardly sustain such a high current density as the fast Li stripping/plating can easily damage the Li/SSE interface by triggering the void formation and dendrite growth. As evidence, cell voltage dramatically increases from 140 to 200 mV in the first discharge and drops to around 0 V at the end of the second cycle (Figure 3f). In contrast, the Li/3D-SSE/Li cell presents stable cyclic performance over 500 h. The flat voltage plateau around 125 mV implies the intact Li/3D-SSE interface during this long-term cycling. Moreover, the Li/3D-SSE/Li cell shows the potential to operate under even lower stack pressure. We conduct another cycling test on the Li/3D-SSE/Li cell in which the applied pressure is gradually released (0.05 MPa per 20 h) after the first 250 h of cycling (Figure 3g). The stable cycling can be maintained until the pressure is reduced to 0.65 MPa after 390 h. After that, the voltage polarization appears, followed by an eventual short circuit after 470 h. To further illustrate the advantage of our design, we compare the applied current density and required stack pressure of the Li/3D-SSE/Li cell in this work to previously reported Li symmetric cells with planar garnet SSEs (Figure 3h).[19,20,35,44,45] Generally, the current density at which the Li/SSE/Li cells can stably operate is in the range of 0.1–0.3 mA cm^{-2}, and the required pressure significantly increases with the current density. Due to the synergistic effect of electrochemical and mechanic modifications from our 3D-SSE, the operating current density can be increased to 0.5 mA cm^{-2} while the required pressure can be reduced to 1.0 MPa, which paves the way to the realization of ASSBs under operating current and pressure needed for practical applications.

We also construct full cells with the 3D-SSE, Li-metal anode, and $LiNi_{0.5}Mn_{0.3}Co_{0.2}O_2$ (NMC) cathode (Figure S8a, Supporting Information). The NMC/3D-SSE/Li cell delivers an initial areal capacity of 1.50 mAh cm^{-2} at a current density of 0.16 mA cm^{-2} (≈0.1 C), about 93.8% of the designed cathode capacity (1.60 mAh cm^{-2}). The areal capacities maintain at 1.41, 1.27, and 1.09 mAh cm^{-2} when the cell is cycled at 0.32, 0.48, and 0.64 mA cm^{-2}, respectively (Figure S8b,c, Supporting Information). The cell can recover to 1.44 mAh cm^{-2} when the applied current density is further reduced from 0.64 to 0.16 mA cm^{-2}. However, the full cell with planar SSE is hard to cycle at 0.48 mA cm^{-2}, as indicated by its micro-shorting behavior shown in the inset (Figure S8b, Supporting Information). Moreover, the full cell maintains capacity retention of 74.3% after 50 cycles at 0.32 mA cm^{-2} (≈0.2 C) (Figure S8d,e, Supporting Information). The excellent rate performance and capacity retention should be attributed to the stable interfacial morphology at the Li/3D-SSE interface.

4. Morphological Evolution at the Interface

We conduct post-mortem analysis to track the morphological evolution at the Li/SSE and Li/3D-SSE interfaces during galvanostatic cycling under 0.2 mA cm^{-2} (0.2 mAh cm^{-2}). Although the pristine Li forms close contact with the SSE before cycling (**Figure 4**a), it becomes partially detached after operation for 30 h (Figure 4b). This morphological degradation incurs a nonuniform stripping/plating at the interface and meanwhile increases the cell voltage, both of which can drive the nucleation and growth of Li dendrites. As shown in the cross-sectional SEM image in Figure 4b and Figure S9 (Supporting Information), Li dendrites have grown into the SSE and caused short-circuit of the cell. The dendrite penetration into SSE can also be optically observed after disassembling the shorted cell and cleaning the SSE surface, as shown as the bright spots contained in the SSE (Figure 4c). Nevertheless, under the same cycling condition, the interfacial morphology in the Li/3D-SSE/Li cell remains almost unchanged over 120 h of cycling (Figure 4d,e). Li metal still firmly contacts with 3D-SSE throughout the entire interface without any voids being present. Furthermore, the intimate contact between Li and 3D-SSE can be maintained after long-term cycling of 500 h under a higher current density of 0.5 mA cm^{-2} (Figure 4f). With excellent morphological stability, the nucleation and penetration of Li dendrites from the interface can be efficiently suppressed, as confirmed by the clean cross-section of the cycled 3D-SSE (Figure 4e,f). This high resistance to Li dendrite growth contributes to the excellent electrochemical performance of the Li/3D-SSE/Li cell shown in previous cycling tests.

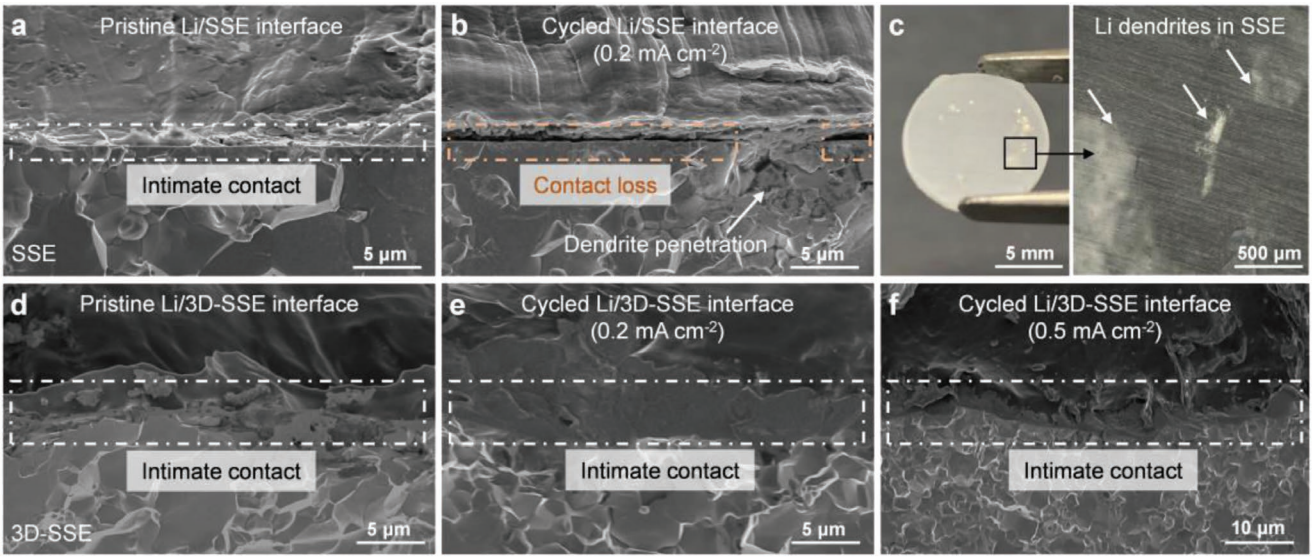

Figure 4. Morphological evolution at the Li/SSE and Li/3D-SSE interfaces. a,b) Cross-sectional SEM images of the Li/SSE interface before (a) and after (b) 30 h of cycling under 0.2 mA cm^{-2} and 1.0 MPa. The pristine Li/SSE interface shows the intact nature, while the cycled interface shows the partially detached morphology. c) Optical images of the SSE disassembled from a shorted Li/SSE/Li cell. The enlarged image shows that the Li dendrites have penetrated the SSE. d,e) Cross-sectional SEM image of the pristine Li/3D-SSE interface (d), the interface after 120 h of cycling under 0.2 mA cm^{-2} (e), and the interface after 500 h of cycling under 0.5 mA cm^{-2} (f). At the cycled Li/3D-SSE interface, Li metal still firmly contacts with 3D-SSE without any voids being present.

We also examine the interfacial morphology for the Li/3D-SSE/Li cell cycled under a releasing pressure (with a cycling profile shown in Figure 3g). When the pressure drops to a certain level, Li striping will dominate the morphological evolution at the interface, which inevitably induces the formation of voids (Figure S10a, Supporting Information). Under such a circumstance, Li dendrites are likely to nucleate at the interface and then penetrate the SSE, causing the short-circuit of the cell. As the path of Li transport between the valleys of two electrodes is shorter, Li prefers to plate or strip at the valley regions. The higher local plating/striping rate promotes the void formation and dendrite nucleation at the valley of 3D patterns instead of the side and top regions (Figure S10b, Supporting Information).

5. Concurrent Electrochemistry and Mechanics at the Interface

Electrochemistry and mechanics are two competing factors in regulating the dynamic evolution of interfacial morphology.[20,46] We perform finite element analysis to understand how the concurrent electrochemistry and mechanics at the interface determine the stability of interfacial morphology upon cell cycling. **Figure 5**a shows an electro-chemo-mechanical model for the Li/3D-SSE/Li cell under galvanostatic cycling (0.5 mA cm^{-2}) and constant stack pressure (1.0 MPa). The loading history and corresponding voltage output can be found in Figure S11 (Supporting Information). The electrochemical and mechanical fields developed in the Li/SSE/Li and Li/3D-SSE/Li cells, such as Li flux in the electrolyte (arrows) and equivalent stress in the Li metal (color contour), are presented in Figure 5b. From an electrochemical perspective, we observe a uniform Li transport in the panel SSE but a nonuniform transport in the 3D-SSE, particularly near the Li/3D-SSE interface. It implies that although the external current densities applied on the cells are the same, the distributions of local current density at the Li/SSE and Li/3D-SSE interfaces are different, as shown in Figure 5c. Herein the numbers 1–5 represent different regions at the Li/3D-SSE interface (also labeled in Figure 5a). With a shorter length of Li transport between two electrodes, region 3 (the valley of 3D patterns with a size of 200 μm) experiences higher local current density and thus faster Li stripping. It indicates that the Li metal at the center of the grids will be much less influenced by this design. Therefore, voids tend to initiate and accumulate at this region when the stack pressure is absent, which is consistent with our experimental observations (Figure S10, Supporting Information). Despite this current singularity at region 3, the local current density passing the Li/3D-SSE interface is still lower than that passing the Li/SSE interface due to the increased effective contact area between Li and 3D-SSE. Therefore, the Li striping and associated electrochemical deformation at the Li/3D-SSE interface is slower, which benefits the stability of interfacial morphology. From a mechanics perspective, we observe a field of higher equivalent stress developed near the Li/3D-SSE interface (Figure 5b). In the detailed stress analysis, we find that the presence of 3D patterns can induce a highly deviatoric stress state in the Li metal near the interface (Figure S12, Supporting Information), which increases the local distortion energy and equivalent stress. Interestingly, we notice that the valley of 3D patterns (region 3) will develop the highest stress to facilitate the Li creep (Figure 5d). Therefore, although the current density for Li stripping/plating at the valley is slightly larger than other regions (Figure 5c), the interfacial morphology can still be maintained well with limited stack pressure, mainly due to the stress effect.

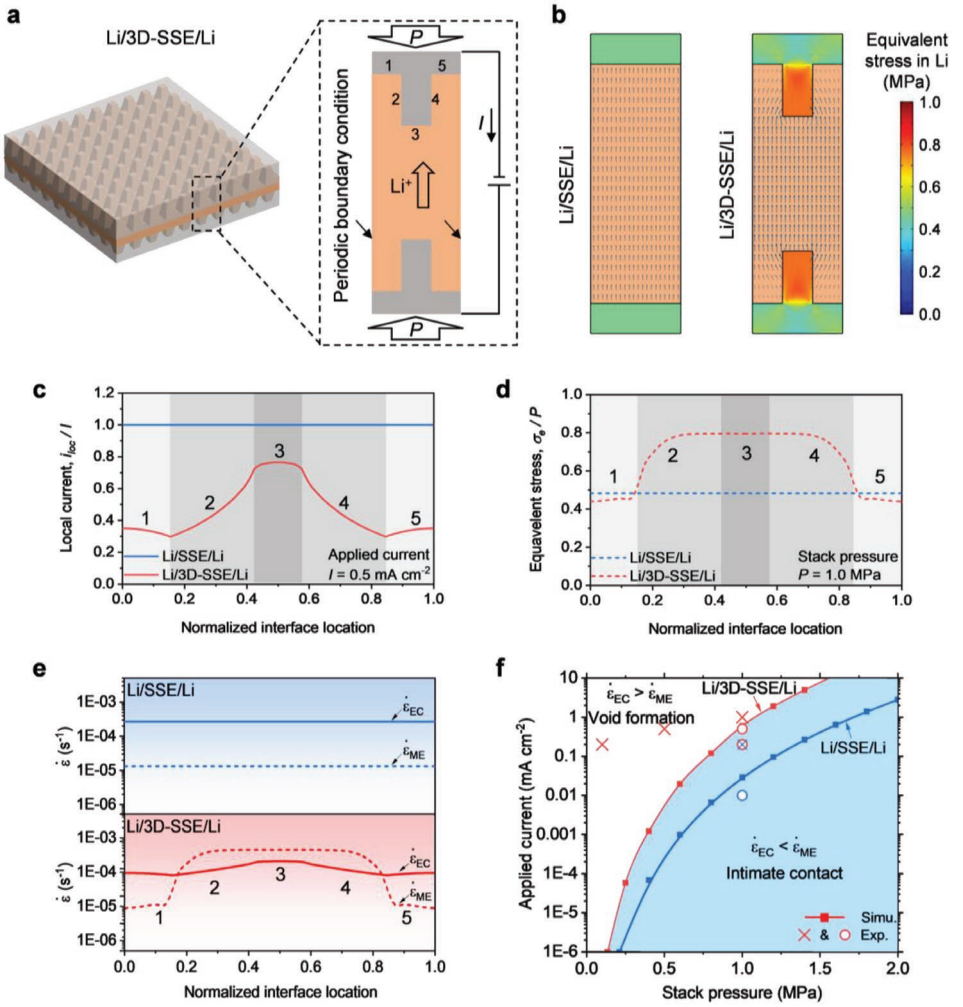

Figure 5. Numerical analysis on the electrochemistry and mechanics at the interface. a) An electrochemomechanical model for Li/3D-SSE/Li cell. b) Distributions of Li flux (arrows) and equivalent stress (color contour) in the Li/SSE/Li and Li/3D-SSE/Li cells cycled under 0.5 mA cm^{-2} and 1.0 MPa. c,d) Distributions of local current density (c) and equivalent stress (d) at the Li/SSE and Li/3D-SSE interfaces. e) Distributions of electrochemical (solid line) and mechanical (dash line) strain rates at the Li/SSE (top) and Li/3D-SSE (bottom) interfaces. f) Phase diagram on the plane spanned by the applied current density and stack pressure to delineate two types of morphological evolution at the interface. Experimental cycling tests using different combinations of current density and stack pressure are also pinned in this diagram. The cross "×" represents the cycling tests terminated by an early short-circuit, and the circle "○" represents the cycling tests lasting for at least 100 h without shorting.

To quantify the competition between electrochemistry and mechanics, we calculate the rates of electrochemical and mechanical deformations ($\dot{\varepsilon}_{EC}$ and $\dot{\varepsilon}_{ME}$, respectively) at the interface based on previous current and stress distributions. At the Li/SSE interface (upper panel in Figure 5e), the $\dot{\varepsilon}_{EC}$ (solid line) is one order magnitude higher than the $\dot{\varepsilon}_{ME}$, indicating the much faster Li striping than the creep. Therefore, the interfacial morphology tends to degrade, leading to void formation, dendrite growth, and eventual short-circuit. At the Li/3D-SSE interface (lower panel in Figure 5e), due to the retarded Li stripping and facilitated Li creep, the $\dot{\varepsilon}_{ME}$ exceeds the $\dot{\varepsilon}_{EC}$ at the most interfacial regions. In this circumstance, the Li mechanically pushed to the interface is sufficient to replenish the Li loss, and therefore the interfacial morphology can remain intact during cell cycling. This quantitative analysis agrees well with our previous experimental observations (Figures 3 and 4) and can be used to further examine the stability of interfacial morphology for the cells cycled under a broader range of current densities and stack pressures. Herein, we construct a phase diagram on a plane spanned by applied current density and stack pressure to delineate two types of morphological evolution at the interface: intimate contact and void formation (Figure 5f). For the cells cycled under low current density and high stack pressure (lower right region), the $\dot{\varepsilon}_{ME}$ is higher than the $\dot{\varepsilon}_{EC}$ such that the cells can stably operate without presenting interfacial degradation. On the other side, when the applied stack pressure is low and the current density is high (upper left region), the $\dot{\varepsilon}_{EC}$ exceeds the $\dot{\varepsilon}_{EC}$, leading to unstable cell cycling and early short-circuit. Note that the boundary between the stable and unstable regions is largely shifted when the 3D-SSE replaces the panel SSE. With the 3D-SSE, the size of the unstable region is reduced, and the stable region occupies more space of the variable plane, indicating the improved morphological stability of the Li/3D-SSE interface. In addition to the theoretical

prediction, experimental cycling tests using different combinations of current density and stack pressure are pinned in this diagram. The cross "×" represents the cycling tests terminated by an early short-circuit due to the interfacial degradation, and the circle "○" represents the cycling tests lasting for at least 100 h without shorting. Cycling tests fall within the predicted stable and unstable regions, demonstrating an excellent consistency between the theoretical prediction and experimental validation.

Our numerical analysis also provides guidelines toward the design of ASSBs with morphologically stable interfaces. We demonstrate that the morphological stability of the Li/3D-SSE interface can be further improved by downsizing the geometric feature of 3D patterns. The distributions of local current density and stress at the interfaces with 3D patterns of various sizes (10, 50, 100, and 200 μm) are shown in Figure S13 (Supporting Information). The interface with smaller patterns experiences lower local current density due to the larger effective contact area between Li and 3D-SSE (Figure S13b, Supporting Information). From the mechanics perspective, the interfacial region with amplified stress expands as the feature size decreases. With these two effects, this interface should present improved morphological stability during cell cycling. To confirm the numerical prediction, we fabricate another two types of 3D-SSE, one with coarser patterns (channel size of 400 μm) and the other one with finer patterns (channel size of 100 μm) (Figure S14, Supporting Information). The electrochemical performance of Li symmetric cells constructed with these two types of 3D-SSE are presented in Figure S15 (Supporting Information). The CCD of Li symmetric cells with 400 μm grids, 200 μm grids, and 100 μm grids are 0.5, 0.7, and 0.8 mA cm^{-2}, respectively, all of which are higher than that of planar SSE (0.3 mA cm^{-2}). The long-term cycling performance is further improved with the reduced pattern size, consistent with our numerical prediction in Figure S13 (Supporting Information).

We also find that small patterns (≈100 μm) can potentially inhibit the Li infiltration into the 3D patterns, leaving the initial gaps between Li metal and 3D-SSE during cell assembling. This side effect might serve as the reason why the performance of the 3D-SSE with finer patterns does not exhibit a dramatic improvement. Moreover, patterning the SSE with a much smaller feature without compromising the quality and cost might be challenging for the current fabrication technique. Novel methods that can fabricate the 3D-SSE precisely and efficiently need to be developed. Slip casting, a well-developed and low-cost technique to form complex shaped ceramics, might be one of the alternative processing methods that can enable the commercial application of our design.[47]

6. Conclusions

We report a novel 3D-SSE with excellent interfacial stability against Li metal based on the synergistic effect of electrochemical and mechanic modifications. This 3D-SSE can reduce the local current density at the interface to retard Li stripping and amplify the mechanical stress near the interface to facilitate Li creep. Therefore, the Li flux toward the interface taken by the fast creep is sufficient to replenish the Li loss caused by the slow stripping, resulting in a morphologically stable interface upon cell cycling. We demonstrate that under limited pressure of 1.0 MPa, the Li symmetric cell using a garnet-type 3D-SSE exhibits a high CCD of 0.7 mA cm^{-2} and stably operates over 500 h at 0.5 mA cm^{-2}. During the cycling, the Li/3D-SSE interface displays an intact nature without any voids and dendrites being present. We further perform finite element analysis to elucidate the competition between electrochemistry and mechanics at the Li/3D-SSE interface, which provides guidelines toward the future design of dendrite-free ASSBs.

7. Experimental Section

Preparation of LLZO SSE: Ta-doped $Li_{6.4}La_3Zr_{1.4}Ta_{0.6}O_{12}$ (LLZO) powder was purchased from MSE Supplies LLC. Dense LLZO pellets were sintered by hot pressing the powder at 1000 °C for 1 h under constant uniaxial pressure of 40 MPa. The density of the sintered LLZO pellets was measured by the Archimedes method. The relative density was determined as the ratio of the measured density and the theoretical density of LLZO (5.17 g cm^{-3}). In this study, the LLZO pellets were 1.6 ± 0.1 mm in thickness and 10.0 mm in diameter. The pellets were first polished with 500, followed by 1000 grit SiC sandpaper using a Buehler EcoMet250 polisher and then transferred into an Ar-filled glovebox for final polishing using 2000 grit SiC sandpaper. The 3D-SSE was fabricated from the polished LLZO pellet using a high-precision laser cutter (Samurai UV Laser Marking System with 354.7 nm wavelength). The pulse duration, transition speed, and cutting cycles of the laser beam were 100 ns, 100 mm s^{-1}, and 200, respectively. After laser cutting, the 3D-SSE was cleaned using a compressed air duster. The cleaned sample was transferred back to the glovebox and heat-treated at 450 °C for 3 h to remove surface contaminations.

Material Characterization: X-ray diffraction (XRD, PANalytical Empyrean with a Cu(Kα) X-ray source) was utilized to examine the phase purity for the SSE and 3D-SSE. Diffraction patterns were collected from 10° to 70° using a step size of 0.01°. Microstructural analysis was performed using a scanning electron microscope (Thermo Fisher Scientific Apreo). An energy-dispersive X-ray spectroscopy (EDS) detector (XFlash 6 | 60 SDD) integrated into the SEM was used to map the elemental distributions. An airtight container was used to transfer the samples from the Ar-filled glovebox to the SEM chamber. X-ray photoelectron spectroscopy (XPS, PHI VersaProbe I with a monochromatized Al(Kα) X-ray Source) was used to characterize the surface chemical compositions for the SSE and 3D-SSE. The mechanical strength of the SSE and 3D-SSE were evaluated by the uniaxial compression test (Instron 5565). The loading rate and maximum load were set as 0.01 1 s^{-1} and 1 kN (equal with a compressive pressure of 12.7 MPa), respectively.

Cell Assembly and Electrochemical Measurements: The ionic conductivity of LLZO pellets was determined by the electrochemical impedance spectroscopy (EIS) measurement with a frequency range from 1 MHz to 0.1 Hz and a perturbation voltage of 10 mV. The Au/SSE/Au blocking cells for EIS measurement were prepared by sputtering thin gold layers (50nm) on both surfaces of the LLZO pellets as two electrodes. The EIS spectra were fit to an equivalent circuit containing two RC components in series representing the bulk and interfacial contributions of the resistance. The EIS measurement was conducted at temperatures ranging from –10 °C to 90 °C in an oven with temperature control. Room-temperature galvanostatic cycling under different current densities was conducted to investigate the CCD and cyclability of Li/3D-SSE/Li and Li/SSE/Li symmetric cells. Li/3D-SSE/Li cells were assembled by sandwiching the 3D-SSE between two Li-metal chips with a thickness of 500 μm. Low-temperature hot pressing was used to improve the initial contact between Li metal and 3D-SSE. Li metals were first pressed onto both sides of the 3D-SSE under a stack pressure of 2.0–3.0 MPa, and the cells were then stored in an oven at 160 °C for several hours without releasing the pressure. The same procedures were used to prepare the Li/SSE/Li cells for comparison. For full cell

fabrication, $LiNi_{0.5}Mn_{0.3}Co_{0.2}O_2$ (NMC) composite cathodes were first prepared by the conventional slurry casting method. 90 wt% NMC powders, 5 wt% carbon black (CB), and 5 wt% polyvinylidene fluoride (PVDF) were mixed in *N*-methyl-2-pyrrolidinone, and then the slurry was cast on Al foil to form a composite electrode with an areal capacity of 1.6 mAh cm^{-2}. For full cell assembling, the 3D-SSE and a Li-metal chip were paired via low-temperature hot pressing. Then, 10 µL of liquid electrolyte (LP40, 1.0 M $LiPF_6$ in EC/ DEC (v/v = 1:1)) was soaked into the composite NMC cathode and served as the ion medium in the cathode and the wetting agent at the interface between cathode and 3D-SSE. All the NMC/3D-SSE/Li cells were operated at an elevated temperature of 40 °C. Before cycling, cells were first charged and discharged with a low current density of 0.1 mA cm^{-2}. All the cells were sealed in pouch cells with Cu strips as current collectors. During cycling, a stack pressure of 1.0 ± 0.05 MPa was applied on the cells using a homemade loading setup. A piezoelectric load cell (OMEGA) was used to adjust the pressure during long-term cycling. Both the EIS measurement and galvanostatic cycling were conducted on a Biologic VMP3 system.

Numerical Simulation: Numerical simulation was performed using COMSOL Multiphysics. A 2D electro-chemo-mechanical model was built to study the concurrent electrochemistry and mechanics at the Li/SSE interface. The electrochemical response of Li symmetric cells was mainly determined by the Li^+ transport in the SSE and the charge transfer reaction at the Li/SSE interfaces. Based on the single-cation conduction mechanism and thus the unity transference number, the Li^+ transport in the inorganic SSE can be described by a simplified Nernst–Planck equation

$$\mathbf{J} = -D_{Li^+}\nabla C_{Li^+} - \frac{\sigma_{Li^+}}{F}\nabla\phi_{SSE} \tag{1}$$

where $\mathbf{J}$ is the Li^+ flux in the electrolyte constituted by diffusion and migration, D_{Li^+} is the Li^+ diffusivity in the electrolyte, C_{Li^+} is the Li^+ concentration in the electrolyte, σ_{Li^+} is the electrolyte conductivity, and φ_{SSE} is the electrolyte potential.[48] At the Li/electrolyte interface, the charge transfer rate of Li dissolution/deposition was calculated based on the potential differences across the Li/SSE interface using the Butler–Volmer equation.

$$i = i_0\left(\exp\left(\frac{\alpha_a F\eta}{RT}\right) - \exp\left(-\frac{\alpha_c F\eta}{RT}\right)\right) \tag{2}$$

where α_a (α_c) is the anodic (cathodic) transfer coefficient, η is the overpotential, and i_0 is the exchange current density. The η is defined as $\eta = \varphi_s - \varphi_{SSE} - E_{eq}$ where φ_s is the electric potential of the electrode, and E_{eq} is the equilibrium potential for the electrochemical reaction (0 V for Li stripping and plating). The i_0 is defined as

$$i_0 = i_{0\_ref}\left(\frac{C_{Li^+}}{C_{Li^+\_ref}}\right)^{\alpha_a} \tag{3}$$

where i_{0_ref} is the reference current density, and $C_{Li^+\_ref}$ is the reference Li^+ concentration in the electrolyte.

The mechanical deformation and stress evolution in the symmetric cells were simulated by the solid mechanics module integrated in the COMSOL software.[49] The constitutive models of LLZO SSE and Li metal were selected as linear elastic and linear-elastic-creep, respectively. For simplification, the mechanical response is decoupled from the electrochemical module such that the initial stripping-induced deformation is assumed to be uniform at the Li/SSE interface (assuming as 1µm Li dissolution). A perfect contact condition, ignoring the friction and adhesion, was employed between Li and SSE. Equivalent stress was calculated and used to represent the driving force for Li creep. Geometrical parameters for the numerical model were set to be consistent with the experimental setup.

The electrochemical ($\dot{\varepsilon}_{EC}$) and mechanical strain rates ($\dot{\varepsilon}_{ME}$) at the interfaces were calculated from the distributions of local current density and stress. Assuming Li ion is the only charge carrier in the LLZO SSE, the current density passing the Li/SSE interface is analogous to the Li flux for deposition/dissolution. Then, $\dot{\varepsilon}_{EC}$, also considered as the rate of thickness change of the electrodes due to Li deposition/dissolution, was given by the equation

$$\dot{\varepsilon}_{EC} = \frac{\dot{\Delta h}}{h} = \frac{i_{loc}M}{\rho F h} \tag{4}$$

where h is the total thickness change in one plating/striping, i_{loc} is the local current density, M is the molar mass of Li, and ρ is the density of Li. $\dot{\varepsilon}_{ME}$ is given by the Norton creep model where the creep strain rate is proportional to a power of the equivalent stress

$$\dot{\varepsilon}_{ME} = A\left(\frac{\sigma_e}{\sigma_{ref}}\right)^n \exp\left(-\frac{Q}{RT}\right) \tag{5}$$

where A is a material parameter, σ_e is the equivalent stress, σ_{ref} is the reference stress, n is the power-law creep exponent, Q is the activation energy, R is the molar gas constant, and T is the temperature. A and n are obtained by converting the creep data from uniaxial tests[50] through the approach proposed by Ma et al.[51] Related physical properties of Li metal and SSE are listed in Table S1 (Supporting Information).

Supporting Information

Supporting Information is available from the Wiley Online Library or from the author.

Acknowledgements

R.X. and F.L. contributed equally to this work. Part of this work was performed at the Stanford Nano Shared Facilities and Stanford Nanofabrication Facility. This work was partially supported by the Assistant Secretary for Energy Efficiency and Renewable Energy, Office of Vehicle Technologies of the U.S. Department of Energy under the Battery Materials Research program and the Battery500 Consortium program.

Conflict of Interest

The authors declare no conflict of interest.

Data Availability Statement

The data that support the findings of this study are available from the corresponding author upon reasonable request.

Keywords

3D-micropatterned garnet, all-solid-state batteries, electrochemomechanics, interfacial degradation, solid-state electrolytes, void formation

Received: May 26, 2021
Revised: September 1, 2021
Published online:

[1] M. Armand, J.-M. Tarascon, *Nature* **2008**, *451*, 652.
[2] C. Martin, *Nat. Nanotechnol.* **2014**, *9*, 327.
[3] I. Hadjipaschalis, A. Poullikkas, V. Efthimiou, *Renewable Sustainable Energy Rev.* **2009**, *13*, 1513.

[4] Y. Ye, L.-Y. Chou, Y. Liu, H. Wang, H. K. Lee, W. Huang, J. Wan, K. Liu, G. Zhou, Y. Yang, A. Yang, X. Xiao, X. Gao, D. T. Boyle, H. Chen, W. Zhang, S. C. Kim, Y. Cui, *Nat. Energy* **2020**, *5*, 786.
[5] A. Kwade, W. Haselrieder, R. Leithoff, A. Modlinger, F. Dietrich, K. Droeder, *Nat. Energy* **2018**, *3*, 290.
[6] D. Lin, Y. Liu, Y. Cui, *Nat. Nanotechnol.* **2017**, *12*, 194.
[7] B. Liu, J.-G. Zhang, W. Xu, *Joule* **2018**, *2*, 833.
[8] X.-B. Cheng, R. Zhang, C.-Z. Zhao, Q. Zhang, *Chem. Rev.* **2017**, *117*, 10403.
[9] J. Liang, J. Luo, Q. Sun, X. Yang, R. Li, X. Sun, *Energy Storage Mater.* **2019**, *21*, 308.
[10] J. C. Bachman, S. Muy, A. Grimaud, H. H. Chang, N. Pour, S. F. Lux, O. Paschos, F. Maglia, S. Lupart, P. Lamp, L. Giordano, Y. Shao-Horn, *Chem. Rev.* **2016**, *116*, 140.
[11] E. J. Cheng, A. Sharafi, J. Sakamoto, *Electrochim. Acta* **2017**, *223*, 85.
[12] L. Porz, T. Swamy, B. W. Sheldon, D. Rettenwander, T. Frömling, H. L. Thaman, S. Berendts, R. Uecker, W. C. Carter, Y.-M. Chiang, *Adv. Energy Mater.* **2017**, *7*, 1701003.
[13] T. Swamy, R. Park, B. W. Sheldon, D. Rettenwander, L. Porz, S. Berendts, R. Uecker, W. C. Carter, Y.-M. Chiang, *J. Electrochem. Soc.* **2018**, *165*, A3648.
[14] T. Krauskopf, R. Dippel, H. Hartmann, K. Peppler, B. Mogwitz, F. H. Richter, W. G. Zeier, J. Janek, *Joule* **2019**, *3*, 2030.
[15] H. Liu, X.-B. Cheng, J.-Q. Huang, H. Yuan, Y. Lu, C. Yan, G.-L. Zhu, R. Xu, C.-Z. Zhao, L.-P. Hou, C. He, S. Kaskel, Q. Zhang, *ACS Energy Lett.* **2020**, *5*, 833.
[16] E. Kazyak, R. Garcia-Mendez, W. S. LePage, A. Sharafi, A. L. Davis, A. J. Sanchez, K.-H. Chen, C. Haslam, J. Sakamoto, N. P. Dasgupta, *Matter* **2020**, *2*, 1025.
[17] D. Wang, C. Zhu, Y. Fu, X. Sun, Y. Yang, *Adv. Energy Mater.* **2020**, *10*, 2001318.
[18] Y. Qi, C. Ban, S. J. Harris, *Joule* **2020**, *4*, 2599.
[19] H. Huo, J. Liang, N. Zhao, X. Li, X. Lin, Y. Zhao, K. Adair, R. Li, X. Guo, X. Sun, *ACS Energy Lett.* **2020**, *5*, 2156.
[20] M. J. Wang, R. Choudhury, J. Sakamoto, *Joule* **2019**, *3*, 2165.
[21] J. Kasemchainan, S. Zekoll, D. S. Jolly, Z. Ning, G. O. Hartley, J. Marrow, P. G. Bruce, *Nat. Mater.* **2019**, *18*, 1105.
[22] T. Krauskopf, H. Hartmann, W. G. Zeier, J. Janek, *ACS Appl. Mater. Interfaces* **2019**, *11*, 14463.
[23] A. Sharafi, H. M. Meyer, J. Nanda, J. Wolfenstine, J. Sakamoto, *J. Power Sources* **2016**, *302*, 135.
[24] H. Koshikawa, S. Matsuda, K. Kamiya, M. Miyayama, Y. Kubo, K. Uosaki, K. Hashimoto, S. Nakanishi, *J. Power Sources* **2018**, *376*, 147.
[25] J. A. Lewis, F. J. Q. Cortes, Y. Liu, J. C. Miers, A. Verma, B. S. Vishnugopi, J. Tippens, D. Prakash, T. S. Marchese, S. Y. Han, C. Lee, P. P. Shetty, H. W. Lee, P. Shevchenko, F. De Carlo, C. Saldana, P. P. Mukherjee, M. T. McDowell, *Nat. Mater.* **2021**, *20*, 503.
[26] Z. Ning, D. S. Jolly, G. Li, R. De Meyere, S. D. Pu, Y. Chen, J. Kasemchainan, J. Ihli, C. Gong, B. Liu, D. L. R. Melvin, A. Bonnin, O. Magdysyuk, P. Adamson, G. O. Hartley, C. W. Monroe, T. J. Marrow, P. G. Bruce, *Nat. Mater.* **2021**, *20*, 1121.
[27] X. Zhang, Q. J. Wang, K. L. Harrison, S. A. Roberts, S. J. Harris, *Cell Rep. Phys. Sci.* **2020**, *1*, 100012.
[28] T. Krauskopf, B. Mogwitz, C. Rosenbach, W. G. Zeier, J. Janek, *Adv. Energy Mater.* **2019**, *9*, 1902568.
[29] J. Cannarella, C. B. Arnold, *J. Power Sources* **2014**, *245*, 745.
[30] X. Wang, W. Zeng, L. Hong, W. Xu, H. Yang, F. Wang, H. Duan, M. Tang, H. Jiang, *Nat. Energy* **2018**, *3*, 227.
[31] J. M. Doux, H. Nguyen, D. H. Tan, A. Banerjee, X. Wang, E. A. Wu, C. Jo, H. Yang, Y. S. Meng, *Adv. Energy Mater.* **2020**, *10*, 1903253.
[32] Y. Xiao, Y. Wang, S.-H. Bo, J. C. Kim, L. J. Miara, G. Ceder, *Nat. Rev. Mater.* **2019**, *5*, 105.
[33] Y. Kim, H. Jo, J. L. Allen, H. Choe, J. Wolfenstine, J. Sakamoto, G. Pharr, *J. Am. Ceram. Soc.* **2016**, *99*, 1367.
[34] J. L. Allen, J. Wolfenstine, E. Rangasamy, J. Sakamoto, *J. Power Sources* **2012**, *206*, 315.
[35] A. Sharafi, E. Kazyak, A. L. Davis, S. Yu, T. Thompson, D. J. Siegel, N. P. Dasgupta, J. Sakamoto, *Chem. Mater.* **2017**, *29*, 7961.
[36] J. Duan, L. Huang, T. Wang, Y. Huang, H. Fu, W. Wu, W. Luo, Y. Huang, *Adv. Funct. Mater.* **2020**, *30*, 1908701.
[37] W. Wu, J. Duan, J. Wen, Y. Chen, X. Liu, L. Huang, Z. Wang, S. Deng, Y. Huang, W. Luo, *Sci. China: Chem.* **2020**, *63*, 1483.
[38] J. Duan, Y. Zheng, W. Luo, W. Wu, T. Wang, Y. Xie, S. Li, J. Li, Y. Huang, *Natl. Sci. Rev.* **2020**, *7*, 1208.
[39] K. Fu, Y. Gong, G. T. Hitz, D. W. McOwen, Y. Li, S. Xu, Y. Wen, L. Zhang, C. Wang, G. Pastel, J. Dai, B. Liu, H. Xie, Y. Yao, E. D. Wachsman, L. Hu, *Energy Environ. Sci.* **2017**, *10*, 1568.
[40] G. T. Hitz, D. W. McOwen, L. Zhang, Z. Ma, Z. Fu, Y. Wen, Y. Gong, J. Dai, T. R. Hamann, L. Hu, E. D. Wachsman, *Mater. Today* **2019**, *22*, 50.
[41] Y. Chen, Z. Wang, X. Li, X. Yao, C. Wang, Y. Li, W. Xue, D. Yu, S. Y. Kim, F. Yang, A. Kushima, G. Zhang, H. Huang, N. Wu, Y. W. Mai, J. B. Goodenough, J. Li, *Nature* **2020**, *578*, 251.
[42] H. Huo, Y. Chen, N. Zhao, X. Lin, J. Luo, X. Yang, Y. Liu, X. Guo, X. Sun, *Nano Energy* **2019**, *61*, 119.
[43] M. Wang, J. B. Wolfenstine, J. Sakamoto, *Electrochim. Acta* **2019**, *296*, 842.
[44] L. Cheng, W. Chen, M. Kunz, K. Persson, N. Tamura, G. Chen, M. Doeff, *ACS Appl. Mater. Interfaces* **2015**, *7*, 2073.
[45] R. H. Basappa, T. Ito, H. Yamada, *J. Electrochem. Soc.* **2017**, *164*, A666.
[46] G. Bucci, T. Swamy, Y.-M. Chiang, W. C. Carter, *J. Mater. Chem. A* **2017**, *5*, 19422.
[47] H. Hassanin, K. Jiang, *Scr. Mater.* **2013**, *69*, 433.
[48] M.-C. Pang, Y. Hao, M. Marinescu, H. Wang, M. Chen, G. Offer, *Phys. Chem. Chem. Phys.* **2019**, *21*, 22740.
[49] R. Xu, Y. Yang, F. Yin, P. Liu, P. Cloetens, Y. Liu, F. Lin, K. Zhao, *J. Mech. Phys. Solids* **2019**, *129*, 160.
[50] W. S. LePage, Y. Chen, E. Kazyak, K.-H. Chen, A. J. Sanchez, A. Poli, E. M. Arruda, M. D. Thouless, N. P. Dasgupta, *J. Electrochem. Soc.* **2019**, *166*, A89.
[51] Y. W. Ma, S. Shim, K. B. Yoon, *Fatigue Fract. Eng. Mater. Struct.* **2009**, *32*, 951.